# Two-axis water-immersible microscanning mirror for scanning optics and acoustic microscopy

Song Xu
Jun Zou

SPIE.

# Two-axis water-immersible microscanning mirror for scanning optics and acoustic microscopy

**Song Xu*** **and Jun Zou**
Texas A&M University, Department of Electrical and Computer Engineering, 188 Bizzell Street, College Station, Texas 77843, United States

**Abstract.** Fast multiaxis scanning is useful for not only optical but also acoustic microscopic imaging. Although they have been used for optical scanning, the application of (MEMS) scanning mirrors in acoustic microscopy is still very limited due to their small mirror plate size, and more importantly, inability to operate in liquids (as ultrasound coupling media). A microfabricated two-axis water-immersible scanning mirror for optical and acoustic microscopy is reported. It has an optical and acoustically reflective mirror plate (6 mm × 4 mm) to provide numerical aperture for ultrasound beam steering. Electromagnetic and mechanical analysis and simulation were conducted to estimate the mechanical tilting angle and resonance frequency of both fast and slow axes, which matches well with the measurement results. The fast axis has a resonant frequency of 320 Hz in air and 220 Hz in water, which is more than 10 times higher than that of the slow axis (24 Hz in air and 14 Hz in water). Under a 100-mA driving current, the scanning angles of the fast axis reached ±9.5 deg in both air and water at the resonance frequency, respectively. The scanning angles of the slow axis reached ±15 deg in air and ±12.5 deg in water at resonant frequencies, respectively. Raster scanning of a collimated laser beam was achieved by driving both axes simultaneously close to their own resonance frequencies. The feasibility of using the two-axis water-immersible scanning mirror in scanning acoustic microscopy was also demonstrated. © *2016 Society of Photo-Optical Instrumentation Engineers (SPIE)* [DOI: 10.1117/1.JMM.15.4.045005]

Keywords: electromagnetic actuator; MEMS mirrors; two-axis; ultrasound; water-immersible.

Paper 16130 received Aug. 12, 2016; accepted for publication Nov. 29, 2016; published online Dec. 21, 2016.

## 1 Introduction

Due to their small form factor and fast scanning speed, microscanning mirrors have been developed for different optical imaging applications, such as optical coherence tomography,[1,2] confocal microscopy,[3] multiphoton microscopy,[4] etc. They can also be useful for scanning acoustic and photoacoustic microscopy by steering focused high-frequency ultrasound beams for pixel-by-pixel data acquisition[5] (Fig. 1). Because high-frequency ultrasound waves cannot propagate effectively in air, it is required that the scanning mirror be submerged in water or other liquids, which serves as an ultrasound coupling medium. However, current microscanning mirrors are mainly designed for free-space optical beam steering in air and therefore are not well suited for underwater operations for ultrasound scanning.[6–9] First, the scanning mirror structures are usually fabricated with brittle silicon-based materials, which could be easily damaged in water due to shock, turbulence, or even imbalance of surface tension. Second, although they are highly efficient in air, the commonly used microactuators, such as electrostatic, piezoelectric and thermal, could easily fail when immersed in water. Third, the small size of the mirror plates limits the achievable numerical aperture and therefore the quality of the reflected light or ultrasound beam.

To address this issue, we have demonstrated a prototype water-immersible two-axis microscanning mirror,[10] which is capable of operating in both air and water. The scanning mirror uses flexible and impact-resistant polymer hinges, instead of brittle silicon ones. It is driven by two electromagnetic microactuators, which can operate efficiently in a liquid environment to generate sufficient driving forces even for a large mirror plate.[11] However, several issues still exist in the design and fabrication of the water-immersible microscanning mirror, which hinders its practical use. For example, the scanning mirror consists of two independent modules for two-axis scanning. The fast-axis scanning module (including the mirror plate, permanent magnets and inductor coil) is directly mounted onto the slow-axis module. Two dangling wires were directly attached to the fast-axis module for supplying driving currents to the inductor coil. As a result, the accuracy and repeatability of the slow axis is greatly affected by the scanning motion of the fast-axis module and also the restriction from the electrical wires. To address the above issues, we report the development of a new water-immersible two-axis microscanning mirror with improved structural design. Its static and dynamic performances in both air and water were estimated with theoretical analysis and numerical modeling and characterized with scanning experiments. The new scanning mirror can achieve more stable and repeatable scanning along both axes. It has a longer lifetime and is much more compact and serviceable, which makes it useful for building compact probes for scanning optical and acoustic imaging applications.[12,13]

## 2 Design and Modeling

Figures 2(a) and 2(b) show the schematic top and side views of the water-immersible two-axis microscanning mirror, respectively. It consists of a silicon substrate as the refractive mirror plate. Aluminum is coated on the polished side of the

---

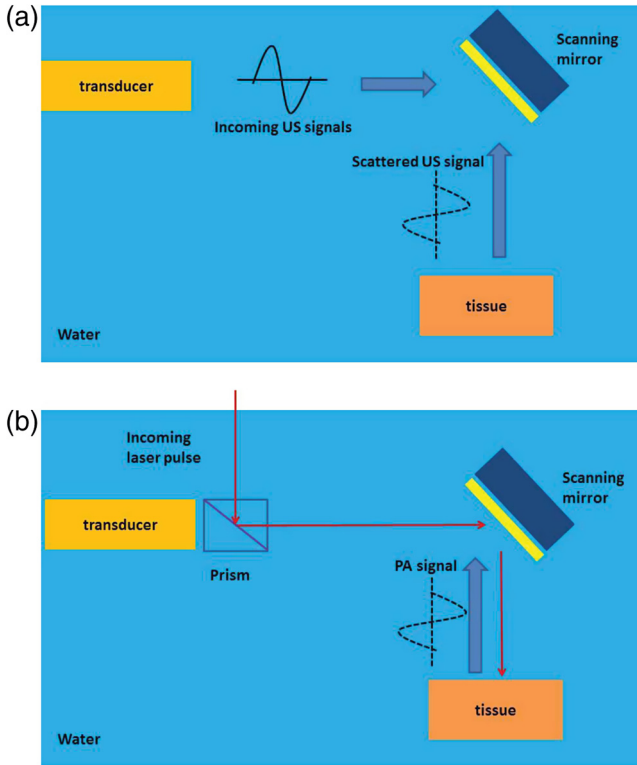*Address all correspondence to: Song Xu, E-mail: xusong.hust@gmail.com

**Fig. 1** (a) Pulse-echo ultrasound scanning and (b) photoacoustic scanning with a water-immersible microscanning mirror.



**Fig. 2** (a) Top-view and (b) side-view of the water-immersible scanning mirror design.

silicon substrate to enhance its optical reflectivity. Because of the large acoustic impedance mismatch (19.7 MRayls for silicon and 1.5 MRayls for water[14]), excellent acoustic reflectivity can also be obtained. The silicon mirror plate is supported on the inner supporting frames by two torsional hinges, which form the primary fast scanning axis. The inner supporting frame is connected to the outer supporting frame by two other torsional hinges, which serve as the secondary (slow) scanning axis. The torsional hinges are made of high-strength biaxially oriented polyethylene terephthalate (BOPET) films. The low stiffness and high fracture strain of BOPET help to reduce the required driving force and also minimize the chance of shock damage in water.

Electromagnetic actuation is selected as the driving mechanism to enable reliable underwater operation. To drive the mirror plate around the fast axis, two permanent magnets with inverse magnetization are fixed to the bottom surface of the mirror plate. An inductor coil is fixed at the center of the plastic holder from underneath.

For the slow axis, two inversely magnetized permanent magnets are fixed to the bottom surface of the inner supporting frame. Two smaller inductor coils are fixed to the plastic holder right below the two permanent magnets. A plastic frame is sandwiched between the outer supporting frame and holder to create a suitable gap between the permanent magnets and inductor coils. When a current flows through the inductor coils, the resultant magnetic field creates a torque on the magnets and therefore rotates the mirror plate around the torsional supporting hinges.

In scanning optical and acoustic microscopy, a raster scanning pattern is desirable for 2-D image reconstruction. To form a raster scanning pattern with good accuracy and
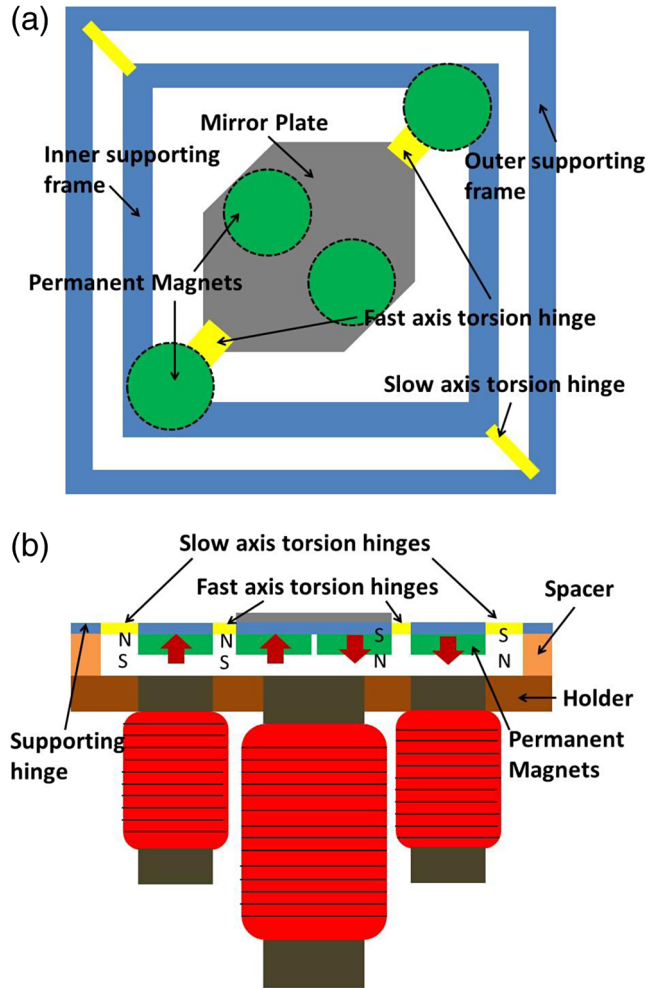
repeatability, the resonant frequencies of the two scanning axes should be significantly different from each other, such that the scanning motion around the two-axes can be largely decoupled. To achieve this, the mirror plate is designed into an oval shape to reduce fluidic damping around the fast axis. The work distance between the two permanent magnets around the slow axis is much larger than that of the fast axis to create higher moment of inertia. In addition, the torsional hinges of the slow axis have a smaller force constant than the fast-axis hinges. The main design parameters of the two-axis microscanning mirror are listed in Table 1.

The mechanical tilting angles of both fast and slow axes under DC driving were estimated. The restoring spring force generated by the BOPET torsion hinges can be calculated by Ref. 16:

$$F_{\text{mechanical}} = \frac{JG}{L'L}\theta, \tag{1}$$

where $\theta$ is tilting angle, $L$ is torsional hinge length, $G$ is shear modulus of torsional hinge, and $J$ is torsional moment of inertia of torsional hinge. For a rectangular beam, $J$ can be calculated as follows:

**Table 1** Main design parameters of water-immersible two-axis microscanning mirror.

|  | Fast axis | Slow axis |
|---|---|---|
| Hinge length (L) | 0.22 mm | 1.4 mm |
| Hinge width (b) | 1.35 mm | 0.5 mm |
| Hinge thickness (h) | 0.2 mm | 0.13 mm |
| Permanent magnet distance (2 × L′) | 5.1 mm | 18.4 mm |
| BOPET hinge shear modulus (G) | 0.12 GPa[15] | |
|  | Permanent magnet | |
| Diameter | 2.6 mm | |
| Height | 0.7 mm | |
|  | Module dimensions | |
| Module length | 16 mm | |
| Module width | 16 mm | |
| Module height | 13 mm | |

$$J = bh^3 \left[ \frac{1}{3} - 0.21 \frac{h}{b} \left( 1 - \frac{h^4}{12b^4} \right) \right]. \quad (2)$$

Due to its distributive and nonlinear nature, the magnetic driving forces generated on the permanent magnets by inductor coils for both fast and slow axes were estimated by using the finite-element method magnetics (FMEM; Fig. 3).[17] The magnetic material and parameters used in the simulation are listed in Table 2. The magnetic force was estimated by using a built-in "Block Integrals" function in FEMM. Figure 4(a) shows the simulated magnetic forces applied onto the two magnets (for driving the fast axis) at different mechanical tilting angles. Since the two magnets are located close to the rotating axis, their travel distance is small even at a large tilting angle. Therefore, the gradient of the magnetic field remains uniform within the entire travel distance, and both magnetic forces increase or decrease almost linearly with the mechanical tilting angle. Figure 4(b) shows the simulated magnetic forces applied onto the two magnets (for driving the slow axis) at different mechanical tilting angles. Since the two magnets are separated farther away from the rotating axis, they have a much larger travel distance when the tilting angle increases. For the magnet moving toward the coil, it is subject to a nonuniform field gradient and therefore, a nonlinear magnetic force. For the other magnet moving away from the coil, it is subject to a more uniform field gradient and therefore, a linear magnetic force. Under DC driving, the mirror plate will stay at its equilibrium position, where the total torque from the two magnetic forces is balanced by the mechanical torque from the supporting hinges (Fig. 5). The cross point of the magnetic and mechanical torque curves denotes the mechanical tilting angle of the mirror plate for a given
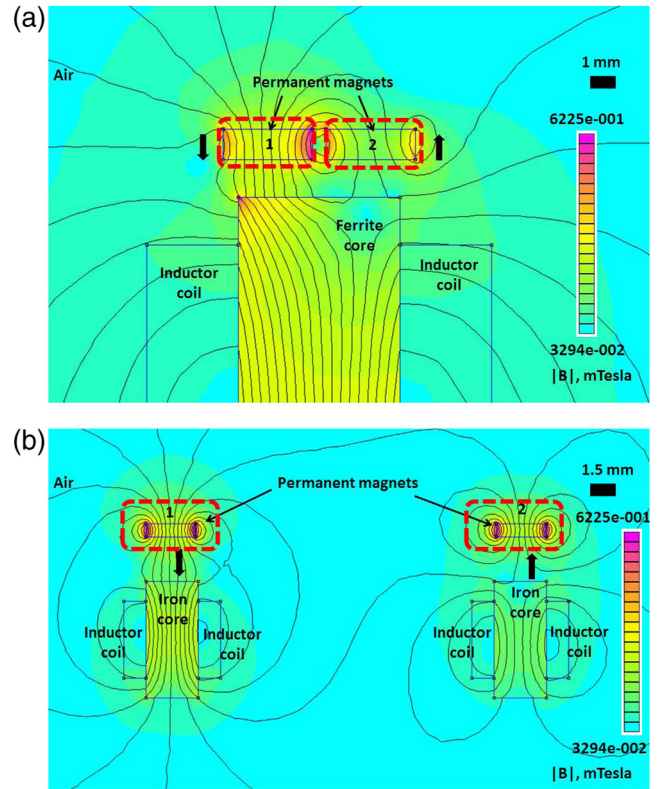


**Fig. 3** FEMM magnetic force simulation: (a) fast axis and (b) slow axis.

**Table 2** FEMM simulation parameters.[a]

| Inductor coils (36 AWG) | Fast-axis coil: 5000 turns |
|---|---|
|  | Slow-axis coil: 3000 turns |
|  | $\mu_x = \mu_y = 1$[b] |
|  | $\sigma = 58 \, \text{MS/m}$[b] |
| DC current | 100 mA |
| Ferrite core (supermalloy) | $\mu_x = \mu_y = 529095$[b] |
|  | $\sigma = 1.7 \, \text{MS/m}$[b] |
|  | $H_c = 0$[b] |
| Iron core (pure iron) | $\mu_x = \mu_y = 14872$[b] |
|  | $\sigma = 10.44 \, \text{MS/m}$[b] |
|  | $H_c = 0$[b] |
| Permanent magnet (N52) | $\mu_x = \mu_y = 1.05$[b] |
|  | $\sigma = 0.667 \, \text{MS/m}$[b] |
|  | $H_c = 891,300 \, \text{A/m}$[b] |

[a]From FEMM library.
[b]$\mu_x$ and $\mu_y$ are the material permeability in horizontal and vertical direction, respectively. $\sigma$ is electrical conductivity. $H_c$ is coercivity. Inductor coil turns are estimated based on coil volume and wire diameter and length.
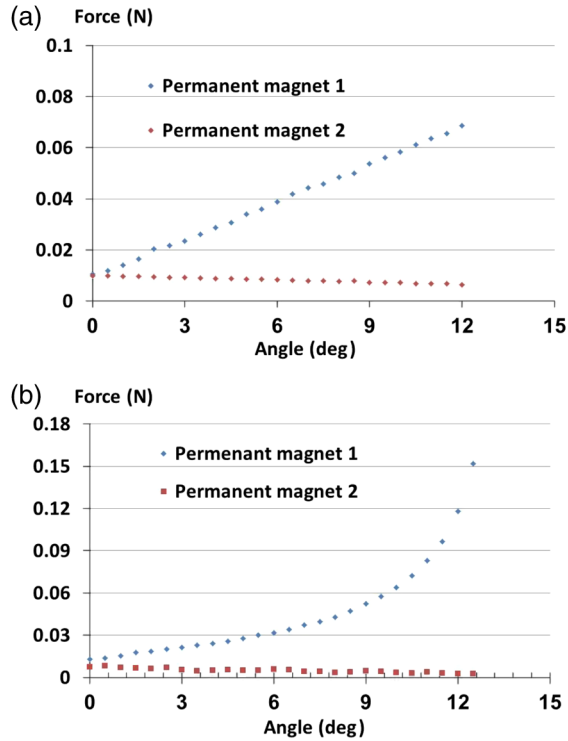
(a)

Force (N)



(b)

Force (N)



**Fig. 4** Simulated magnetic forces on the two permanent magnets: (a) fast axis and (b) slow axis.

(a)

Torque (N-mm)



(b)

Torque (N-mm)



**Fig. 5** Simulated magnetic and spring torques: (a) fast axis and (b) slow axis.

DC driving current. It should be noted that due to the different magnitudes of the two magnetic forces, there will be a nonzero transverse force existing on the torsion hinge, which could cause vertical bending of the torsion hinges and therefore vibration of the mirror plate. However, because the torsion hinges are designed to have short lengths and therefore high bending stiffness, such vertical bending and displacement will be largely suppressed and should not affect the scanning motion of the two axes.

Based on the geometric and mechanical parameters of the BOPET hinges, the scanning resonance frequencies of both fast and slow axes were estimated.

The governing equation for the torsional oscillation of a beam structure is as follows:

$$I\frac{d^2\theta}{dt^2} + C\frac{d\theta}{dt} + K\theta = \tau(t), \tag{3}$$

where $I$ is the moment of inertia, $K$ is the coefficient of torsion spring, $C$ is the rotational friction (damping), $\tau(t)$ is the applied torque per unit length along the beam, and $t$ is time. Since damping in air is small ($C \ll \sqrt{\frac{K}{I}}$), the frequency of vibration is very near the natural resonant frequency:

$$f_{air} = \frac{1}{2\pi}\sqrt{\frac{K}{I}}. \tag{4}$$

The resonance frequency in fluid can be estimated from that in vacuum as Ref. 18:

$$f_{water} = f_{air}\left[1 + \frac{3\pi}{2\rho h}\Gamma_t(n)\right]^{-1/2}, \tag{5}$$

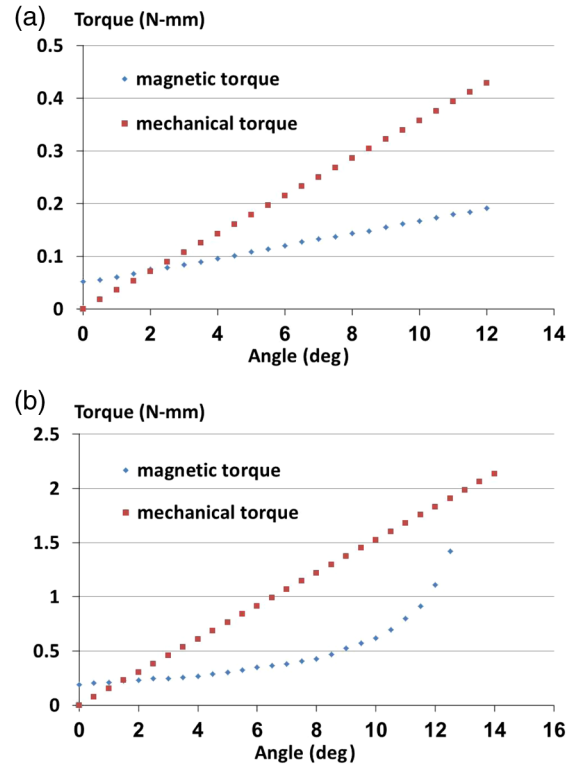where $\rho$ is water density and $\Gamma_t(n)$ is the hydrodynamic function for torsional oscillations, which can be estimated from Pade approximants:

$$\Gamma_t(n) = \frac{1}{16}\left(\frac{1 + 0.37922\kappa + 0.072912\kappa^2}{1 + 0.37922\kappa + 0.088056\kappa^2 + 0.010737\kappa^3}\right), \tag{6}$$

where $\kappa$ is normalized mode number:

$$\kappa = \frac{\pi}{2}(2n-1)\frac{b}{L}. \tag{7}$$

In our case, only first-order resonant ($n = 1$) is considered. Resonance frequencies of both fast and slow axes in air and water can be calculated according to Eqs. (4)–(7). Simulated DC steering angles and calculated resonant frequencies are listed in Table 3.

**Table 3** Estimated resonance frequencies and simulated tilting angles.

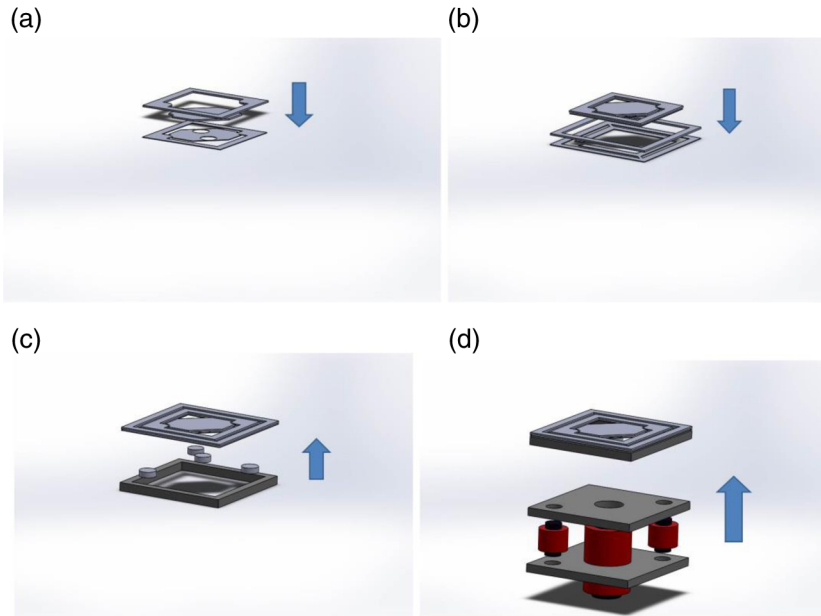|  | Fast axis | Slow axis |
|---|---|---|
| $f_{air}$ | 331 Hz | 20 Hz |
| $f_{water}$ | 249 Hz | 13 Hz |
| $\theta_{air}$ at 100 mA DC | 2 deg | 1.5 deg |

**Fig. 6** (a) Mirror plate and inner frame attached to BOPET hinge structure, (b) outer frame attached to inner frame, (c) magnets and spacer attached, and (d) inductor actuators attached.
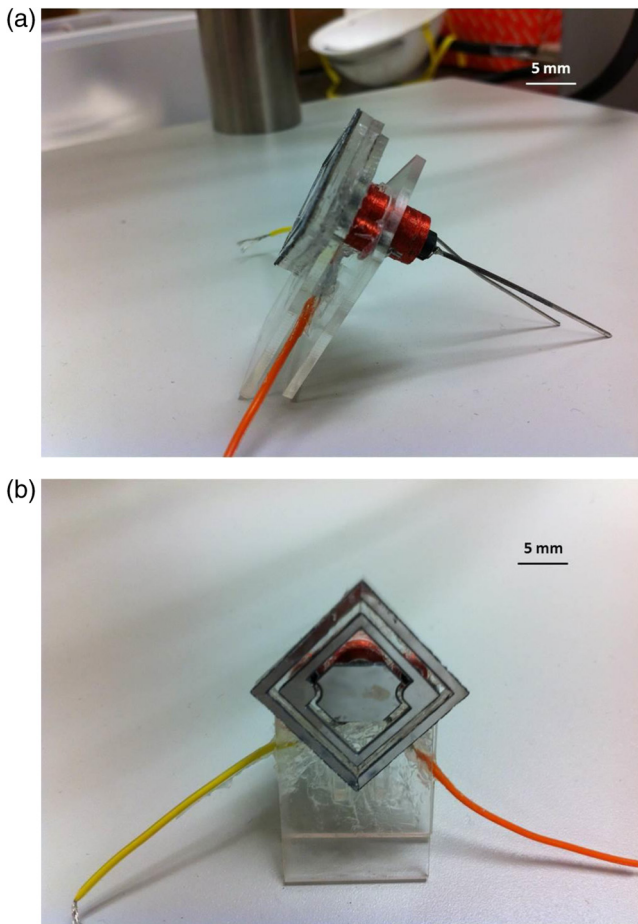


**Fig. 7** Assembled two-axis water-immersible scanning mirror (a) side view and (b) front view.
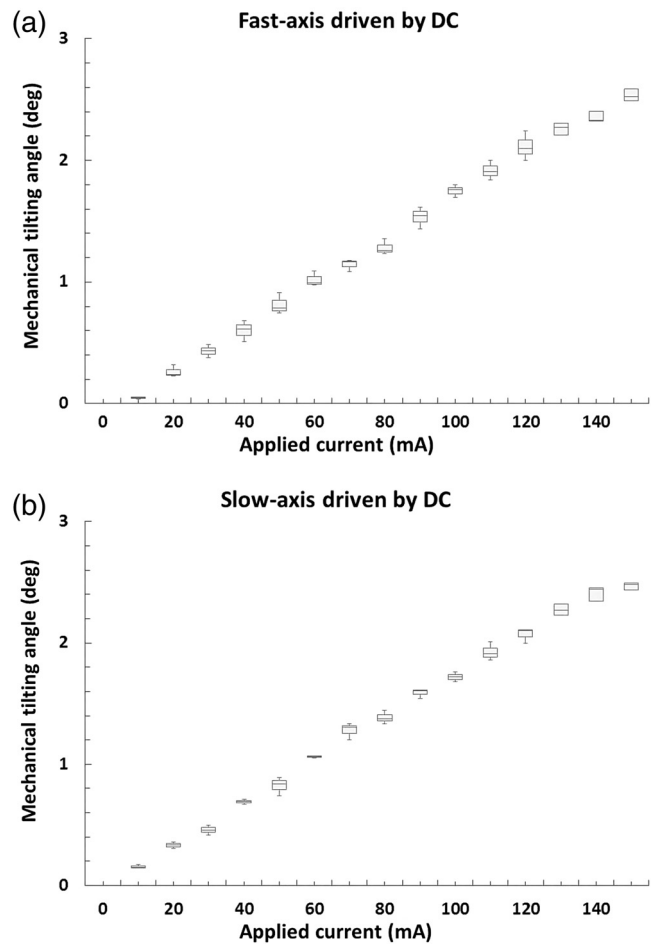


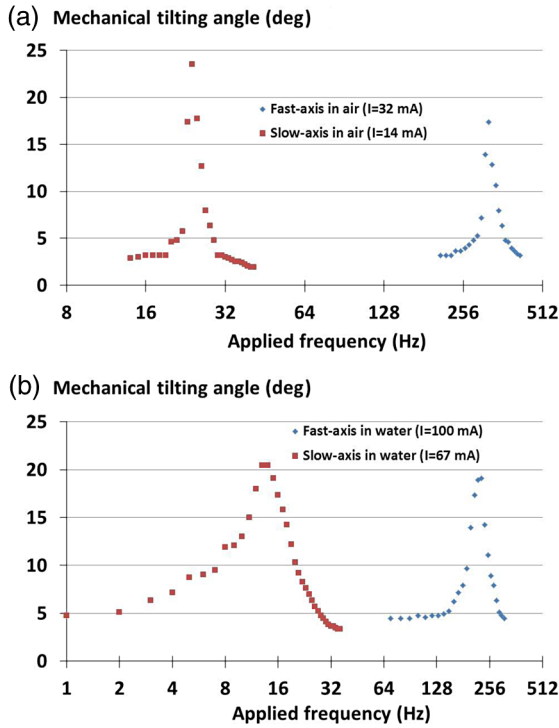**Fig. 8** DC test results on (a) fast-axis module and (b) slow-axis module.

(a) Mechanical tilting angle (deg)

Fast-axis in air (I=32 mA)
Slow-axis in air (I=14 mA)

Applied frequency (Hz)

(b) Mechanical tilting angle (deg)

Fast-axis in water (I=100 mA)
Slow-axis in water (I=67 mA)

Applied frequency (Hz)

**Fig. 9** Resonant frequency test in (a) air and (b) water.

## 3 Fabrication and Characterization

The fabrication of the water-immersible microscanning mirror is conducted as follows (Fig. 6). First, the reflective mirror plate was etched out from a polished single-crystalline silicon wafer with deep reactive-ion etching (PlasmaLab System 100, Oxford). A thin layer of aluminum (70 nm) is deposited onto the silicon mirror surface with e-beam evaporation (PVD 75, Lesker) to enhance its optical reflectivity. Second, the torsional hinges and frames were trimmed from a 130-$\mu$m-thick BOPET film and a 1.5-mm-thick acrylic sheet, respectively, by using a laser cutting machine (PLS6.57, Universal Laser System). After all the components were fabricated, the silicon mirror plate, supporting frame, NdFeB grade N52 permanent magnetic discs (D101-N52, K&J Magnetics), BOPET torsional hinges, and inductor coils (70F332AF-RC, 33 mH and 70F103AI-RC, 1 mH, BOURNS) were assembled and bonded together with silicone rubber adhesive (RTV 108, Momentive Performance Materials). Figure 7 shows a fully assembled two-axis water-immersible scanning mirror. It has an overall length, width, and thickness of 16, 16, and 13 mm, respectively.

A laser tracing method was used to characterize the mechanical tilting angle ($\theta$) and resonant frequency ($f$) in both air and water. The scanning mirror was fixed in a water tank. A CW laser beam was projected at the center of the mirror plate at an incident angle of 45 deg. The
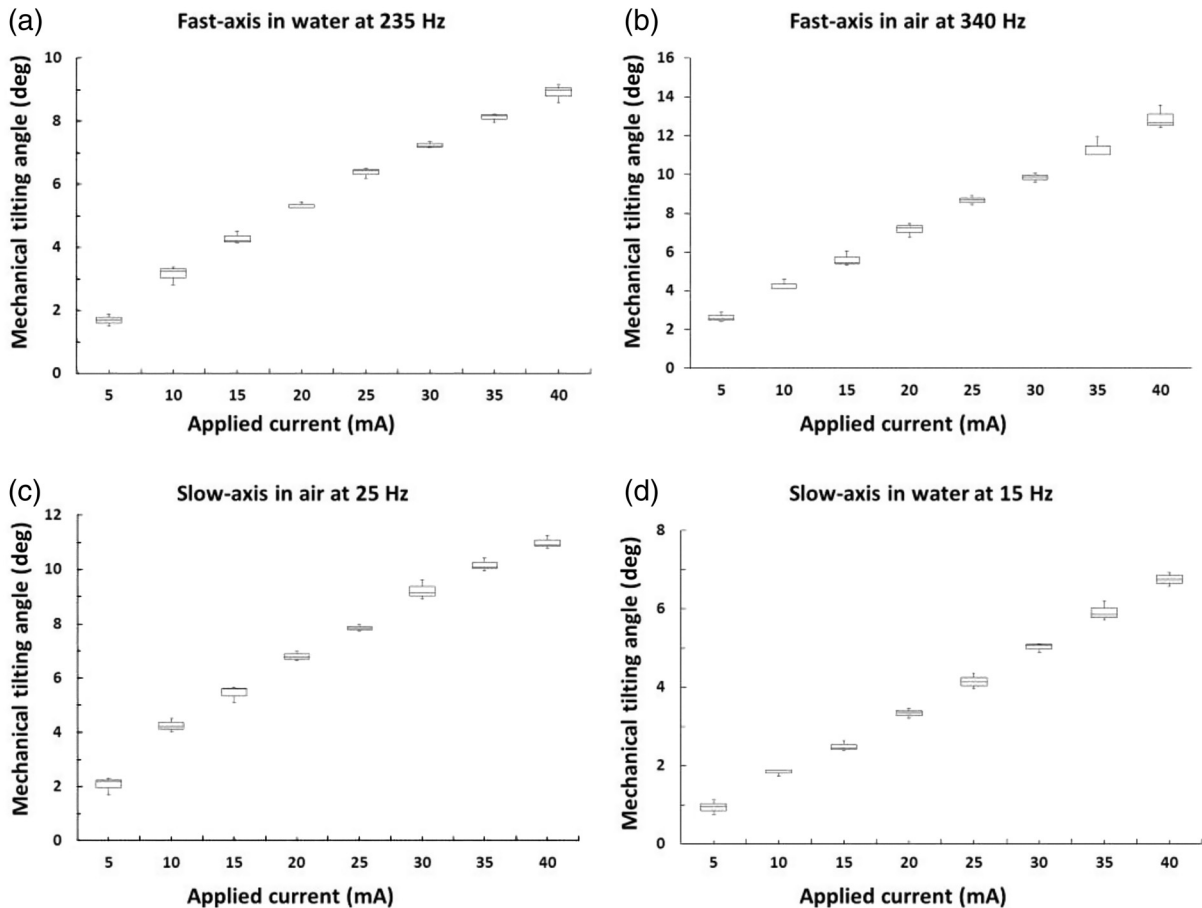


(a) Fast-axis in water at 235 Hz

(b) Fast-axis in air at 340 Hz

(c) Slow-axis in air at 25 Hz

(d) Slow-axis in water at 15 Hz

**Fig. 10** AC test results at resonance frequencies.

**Table 4** Applied driving currents in raster scanning tests.

| | Air | Water | Mechanical angles (deg) |
|---|---|---|---|
| Fast axis | 32 mA; 300 Hz | 100mA; 190 Hz | 12 |
| Slow axis | 14 mA; 25 Hz | 100 mA; 19 Hz | 17 |



**Fig. 11** (a) Raster scanning test result in air and (b) raster scanning test result in water.

mechanical tilting angle was calculated based on the length of the laser scanning trace on a ruler placed at 60 mm away from the mirror plate. Under DC driving, the mechanical tilting angle of both the fast and the slow axes increases almost linearly with the driving current. Figure 8 shows the average and standard deviation of the mechanical tilting angle obtained from three measurements. With a DC driving current of 100 mA, the mechanical tilting angle of the fast and slow axes reached 1.75 and 1.7 deg, respectively, which match well with the simulated values. With an AC driving current of 100 mA, the mechanical tilting angle of the fast and slow axes at different frequencies was also characterized to identify their resonance frequencies. The scanning resonant frequency is defined as the frequency at which the scanning angle reaches its maximum when the scanning mirror is driven by an AC current with fixed amplitude but different frequencies. As shown in Fig. 9, the resonance frequencies of the fast and slow axes in air were determined to be 320 and 24 Hz, respectively. Their resonance frequencies in water were determined to be 220 and 14 Hz, respectively. In addition, the mechanical tilting angle of the fast and slow axes under AC driving was characterized. The fast axis was driven at its resonance frequencies with different current amplitude in air and water [Figs. 10(a) and 10(b)]. The same test was conducted on the slow axis [Figs. 10(c) and 10(d)]. It can be observed that the mechanical tilting angle increases almost linearly with respect to the applied current amplitude. To test the scanning reliability, both the fast and slow axes were driven in water at their resonant frequencies for over 10 million cycles, respectively. No noticeable shift in scanning angle and resonance frequency was observed.

Raster scanning with both axes actuated was also tested by using the laser tracing method in air and water, respectively. The amplitude and frequency of the AC driving currents and the resulting mechanical tilting angles of the fast and slow axes are listed in Table 4. Both driving currents were synchronized and their phases were locked. The raster scanning patterns of the scanning mirror when it is placed in air and water are shown in Figs. 11(a) and 11(b), respectively. In air, the driving frequency of the fast axis is 12 times that of the slow axis. Therefore, in the raster scanning pattern, a half slow scanning cycle consists of six fast ones. In water, the driving frequency of the fast axis is 10 times that of the slow axis. Therefore, a half slow scanning cycle consists of five fast ones. It should be noted that in both raster scanning patterns, there is a slight vertical shift in the fast scanning cycles. This is because when the slow axis is actuated, the orientation of the two magnets used to drive the fast axis will be tilted. This changes the balance of the electromagnetic forces between the two magnets and the inductor coil. However, as shown in Fig. 11, both raster scanning patterns are stable and repeatable. Therefore, once the scanning
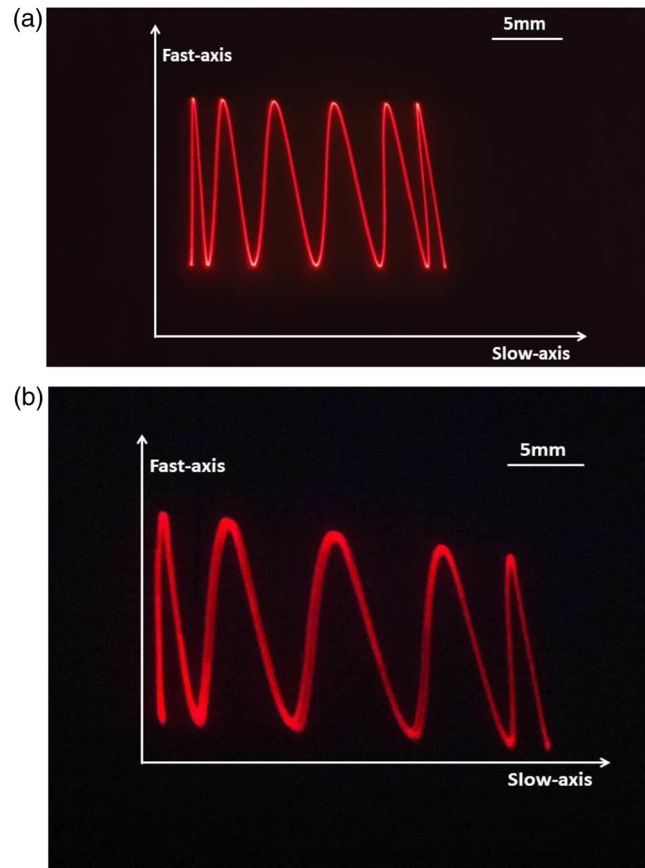
path is calibrated, this shift should not be a big concern for real applications.

## 4 Ultrasound Imaging Experiment

The imaging setup consists of a water tank, a high frequency (25 MHz) focused ultrasound transducer (V324-SM-F2.00IN-PTF, Olympus) with a focal length of 50.4 mm, and the water-immersible microscanning mirror and three 0.9-mm pencil leads as target (Fig. 12). The scanning mirror
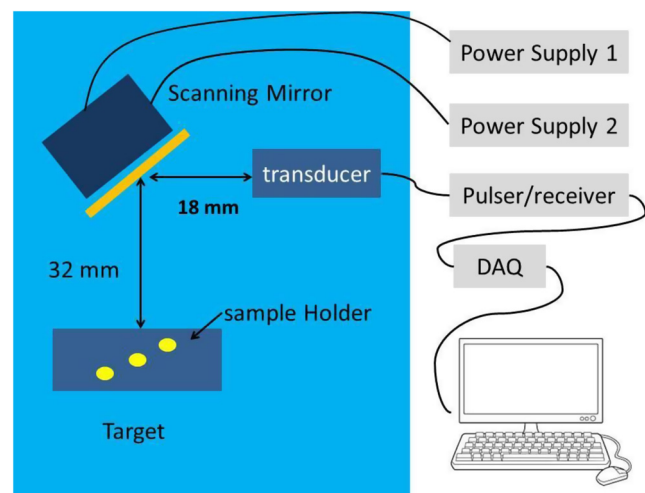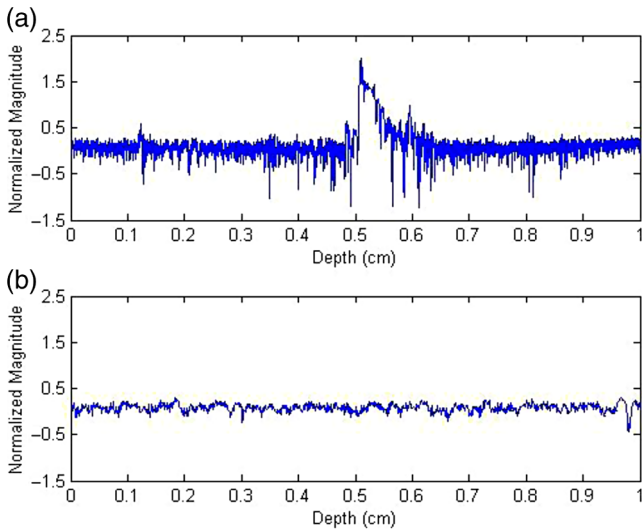


**Fig. 12** Ultrasound imaging test setup.

**Fig. 13** (a) Target A-line and (b) background A-line.

was placed 18 mm away from the transducer at an angle of 45 deg. The target was located 32 mm away from the center of the mirror plate, such that they are located in the focal zone of the ultrasound transducer. The ultrasound transducer was connected to a pulser/receiver system (5072PR, Olympus) and an oscilloscope (TDX 2014B, Tektronix). The pulse repetition rate and pulse width were set to be 5 kHz and 1 ns, respectively. A function generator and a custom-build current amplifier were used to supply AC currents to drive the scanning mirror. A data acquisition card (PCI6251, National Instruments) was used to collect the backscattered ultrasound signals from the target. A LabView (National Instruments) program was developed to synchronize the scanning and data acquisition. The fast axis was driven by a current of 100 mA AC at 50 Hz, which provides a $\pm 1.5$-mm scanning range. At a pulse-echo repetition rate of 5 kHz, a total number of 50 scan points was distributed along the entire scanning path. At each scan point, the transducer sent an ultrasound pulse and detected the backscattered signal (A-line; Fig. 13).
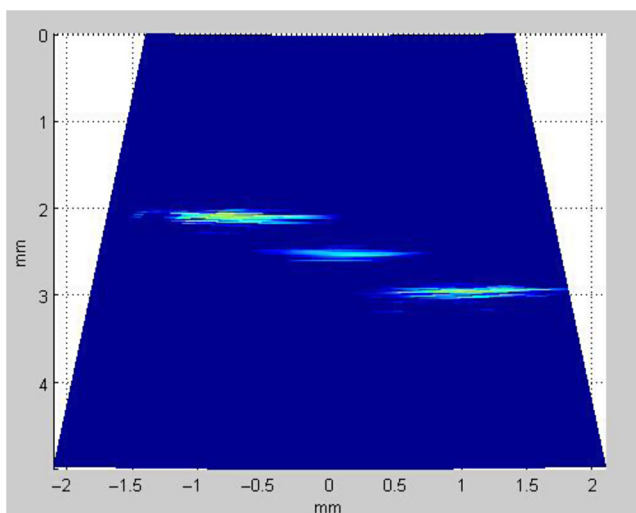


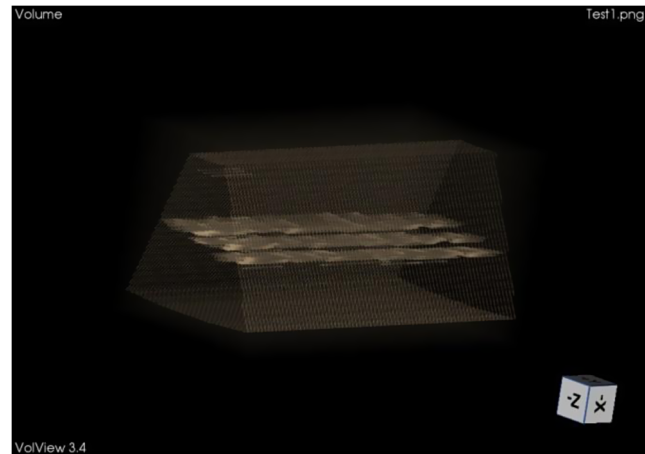**Fig. 14** B-mode images of fast axis.



**Fig. 15** 3-D ultrasound image.

The slow axis was driven by a linearly increased DC current with an increment of 10 mA for 20 steps, which provides 20 scanning planes within 2 mm. For image reconstruction, each A-line was averaged 15 times. The 50 A-line along each fast scanning path was stacked to form a 2-D B-mode image. The resolution and contrast of the B-mode image were further improved with a synthetic aperture focusing technique[19] (Fig. 14). The 2-D B-mode images were further stacked along the slow-axis scanning direction ($z$-direction) to form a 3-D volumetric image (Fig. 15). The relative location of the three imaging targets in the reconstructed ultrasound images matches well with their actual arrangement in the imaging setup. The $-6$ dB width of the imaging targets was determined to be 1312 $\mu$m, which is larger than their nominal width of 0.9 mm. This is caused by the relatively large focal spot size ($\sim 1$ mm) of the transducer and the relatively few (only 50) data points along the scan path. By using a transducer with a smaller focal spot and a pulser–receiver with higher repetition rate, the lateral resolution of the ultrasound images can be further improved for better estimation of the target size.

## 5 Conclusion

In conclusion, a new two-axis water-immersible microscanning mirror has been developed. It inherits the fast and wide-field underwater scanning capability of its predecessor. With an improved structural design, the coupling of the two scanning axes has largely been eliminated, which allows a stable and repeatable dynamic raster scanning pattern to be achieved with both axes driven at their own resonance frequencies. Its unique scanning capability can be useful for development of miniaturized scanning optical and acoustic imaging for hand-held operations.

## References

1. P. M. Hagelin et al., "Scalable optical cross-connect switch using micromachined mirrors," *IEEE Photonics Technol. Lett.* **12**(7), 882–884 (2000).
2. V. X. Yang et al., "Doppler optical coherence tomography with a micro-electro-mechanical membrane mirror for high-speed dynamic focus tracking," *Opt. Lett.* **31**(9), 1262–1264 (2006).
3. H. Ra et al., "Two-dimensional MEMS scanner for dual-axes confocal microscopy," *J. Microelectromech. Syst.* **16**(4), 969–976 (2007).
4. W. Jung et al., "Miniaturized probe based on a microelectromechanical system mirror for multiphoton microscopy," *Opt. Lett.* **33**(12), 1324–1326 (2008).
5. L. Lin et al., "Hand-held optical-resolution photoacoustic microscopy," *J. Biomed. Opt.* **22**(2), 041002 (2016).
6. K. H. Koh and C. Lee, "A two-dimensional MEMS scanning mirror using hybrid actuation mechanisms with low operation voltage," *J. Microelectromech. Syst.* **21**(5), 1124–1135 (2012).
7. I.-J. Cho and E. Yoon, "A low-voltage three-axis electromagnetically actuated micromirror for fine alignment among optical devices," *J. Micromech. Microeng.* **19**(8), 085007 (2009).
8. K. H. Kim et al., "Two-axis magnetically-driven MEMS scanning catheter for endoscopic high-speed optical coherence tomography," *Opt. Express* **15**(26), 18130–18140 (2007).
9. L. Xi et al., "Photoacoustic imaging based on MEMS mirror scanning," *Biomed. Opt. Express* **1**(5), 1278–1283 (2010).
10. C.-H. Huang et al., "A water-immersible 2-axis scanning mirror microsystem for ultrasound andha photoacoustic microscopic imaging applications," *Microsyst. Technol.* **19**(4), 577–582 (2013).
11. D. Niarchos, "Magnetic MEMS: key issues and some applications," *Sens. Actuators A* **109**(1), 166–173 (2003).
12. J. Yao et al., "Label-free oxygen-metabolic photoacoustic microscopy in vivo," *J. Biomed. Opt.* **16**(7), 076003 (2011).
13. J. Y. Kim et al., "Fast optical-resolution photoacoustic microscopy using a 2-axis water-proofing MEMS scanner," *Sci. Rep.* **5**, 7932 (2015).
14. L. E. Kinsler and A. R. Frey, *Fundamentals of Acoustics*, 2nd ed., Wiley, New York (1962).
15. Engineering Toolbox, "Modulus rigidity," http://www.engineeringtoolbox.com/ (2001).
16. Y. Zhang et al. "Design and analysis of the micromechanical structure for an electromagnetic bistable RF MEMS switch," in *Asia-Pacific Microwave Conf. Proc.*, Vol. 1, IEEE (2005).
17. D. C. Meeker, "Improvised asymptotic boundary conditions for electrostatic finite elements," *IEEE Trans. Magn.* **50**(6), 1–9 (2014).
18. C. A. Van Eysden and J. E. Sader, "Resonant frequencies of a rectangular cantilever beam immersed in a fluid," *J. Appl. Phys.* **100**(11), 114916 (2006).
19. C. H. Frazier and W. D. O'Brien, "Synthetic aperture techniques with a virtual source element," *IEEE Trans. Ultrasonics Ferroelectr. Freq. Control* **45**(1), 196–207 (1998).

**Song Xu** received his BS in optical and electrical engineering from Huazhong University of Science and Technology, China in 2012. He is currently pursuing the PhD in the Department of Electrical and Computer Engineering at Texas A&M University. His current research involves building MEMS scanning mirrors for SAM and PAM and ultrasound image reconstruction.

**Jun Zou** (M'09-SM'15) received his PhD in electrical engineering from the University of Illinois at Urbana-Champaign in 2002. In 2004, he joined the Department of Electrical and Computer Engineering at Texas A&M University, where he is currently an associate professor. His current research interests lie in the development of micro and nano opto-electro-mechanical devices and systems for biomedical imaging and sensing applications.